

FIRST IDENTIFICATION OF 10-kpc SCALE [C II] 158 μ m HALOS
AROUND STAR-FORMING GALAXIES AT $z = 5 - 7$ SEIJI FUJIMOTO¹, MASAMI OUCHI^{1,2}, ANDREA FERRARA^{3,4}, ANDREA PALLOTTINI³,
R. J. IVISON^{5,6}, CHRISTOPH BEHRENS³, SIMONA GALLERANI³,*Submitted to ApJ*

ABSTRACT

We report the discovery of 10-kpc scale [C II] 158 μ m halos surrounding star-forming galaxies in the early Universe. We choose deep ALMA data of 18 galaxies each with a star-formation rate of $\simeq 10 - 70 M_{\odot}$ with no signature of AGN whose [C II] lines are individually detected at $z = 5.153 - 7.142$, and conduct stacking of the [C II] lines and dust-continuum in the uv -visibility plane. The radial profiles of the surface brightnesses show a 10-kpc scale [C II] halo at the 9.2σ level significantly extended more than the HST stellar continuum data by a factor of ~ 5 on the exponential-profile scale length basis, as well as the dust continuum. We also compare the radial profiles of [C II] and Ly α halos universally found in star-forming galaxies at this epoch, and find that the scale lengths agree within the 1σ level. The existence of the extended [C II] halo is the evidence of outflow remnants in the early galaxies and suggest that the outflows may be dominated by cold-mode outflows, which challenges current galaxy evolution models.

Keywords: galaxies: formation — galaxies: evolution — galaxies: high-redshift

1. INTRODUCTION

Galaxy size and morphological studies in the early Universe provide important insights into the initial stage of galaxy formation and evolution. The size and morphology in the rest-frame ultra-violet (UV) and far-infrared (FIR) wavelengths trace the areas of young star formation and the active starbursts that are less and heavily obscured by dust, respectively. The [C II] $^2P_{3/2} \rightarrow ^2P_{1/2}$ fine-structure transition at 1900.5469 GHz (157.74 μ m) is a dominant coolant of the inter-stellar medium (ISM) in galaxies (e.g., Stacey et al. 1991; De Looze et al. 2014), whose size and morphology are strong probes of ISM properties. Comparing the size and morphology in the rest-frame UV+FIR continuum and the [C II] 158- μ m line is thus important to comprehensively understand the evolutionary process via the star-formation surrounded by the ISM.

The *Hubble Space Telescope* (HST) has revealed the size and morphological properties in the rest-frame UV wavelengths for the high-redshift galaxies up to $z \sim 10$ (e.g., Oesch et al. 2010; Ono et al. 2013; Shibuya et al. 2015; Bouwens et al. 2017; Kawamata et al. 2018). These HST studies show that star-forming galaxies generally have an exponential-disk profile and become compact toward high redshifts.

The Atacama Large Millimeter / submillimeter

Array (ALMA) has opened our views to the obscured star-formation and the [C II] line properties in the rest-frame FIR wavelength up to $z \sim 7$ (e.g., Watson et al. 2015; Maiolino et al. 2015; Capak et al. 2015; Pentericci et al. 2016; Knudsen et al. 2016; Matthee et al. 2017; Carniani et al. 2018; Smit et al. 2018; Bowler et al. 2018). There have also been several attempts to measure the size and morphology in the rest-frame FIR continuum and the [C II] line for such high redshift galaxies at $z \sim 5-7$, where Carniani et al. (2017) report that the effective radius of the [C II] line-emitting region is larger than that of the rest-frame UV region. However, large uncertainties still remain due to the small number statistics and observational challenges.

One critical challenge is sensitivity. The recent ALMA studies show that signal-to-noise ratio (S/N) > 10 is needed to obtain reliable size measurement results both on the image-based and visibility-based analyses (e.g., Simpson et al. 2015; Ikarashi et al. 2015), while the majority of the previous ALMA detections of the dust continuum and the [C II] line from $z \sim 5-7$ galaxies show the S/N less than 10. If the S/N level is poor, noise fluctuations significantly affect the profile fitting results. Moreover, Hodge et al. (2016) show that the combination of the original smoothed galaxy profile and the noise fluctuations can make the morphology more clumpy. To obtain the reliable size and morphological results, extensively deep observations are thus required.

In this paper, we determine the size and morphology for the dust continuum and the [C II] line in the star-forming galaxies at $z = 5 - 7$ via the stacking technique in the uv -visibility plane, utilizing new and archival deep ALMA Band 6/7 data. In conjunction with deep HST images, we study the general morphology of the total star-formation and the ISM in the epoch of re-ionization. The structure of this paper is as follows. In Section 2, the observations and the data reduction are described.

sfseiji@icrr.u-tokyo.ac.jp

¹ Institute for Cosmic Ray Research, The University of Tokyo, Kashiwa, Chiba 277-8582, Japan² Kavli Institute for the Physics and Mathematics of the Universe (WPI), University of Tokyo, Kashiwa 277-8583, Japan³ Scuola Normale Superiore, Piazza dei Cavalieri 7, I-56126 Pisa, Italy⁴ Centro Fermi, Museo Storico della Fisica e Centro Studi e Ricerche "Enrico Fermi" Piazza del Viminale 1, Roma, 00184, Italy⁵ European Southern Observatory, Karl Schwarzschild Str. 2, D-85748 Garching, Germany⁶ Institute for Astronomy, University of Edinburgh, Royal Observatory Blackford Hill, Edinburgh EH9 3HJ, UK

Section 3 outlines the method of [CII] line detections, line velocity width, source position measurements, and the stacking processes of ALMA and HST data. We report the results of the radial profiles of the [CII] line, rest-frame FIR, and rest-frame UV wavelengths in Section 4. In Section 5, we discuss the physical origin of the extended [CII] line emission, comparing with the zoom-in cosmological simulation results. A summary of this study is presented in Section 6.

Throughout this paper, we assume a flat universe with $\Omega_m = 0.3$, $\Omega_\Lambda = 0.7$, $\sigma_8 = 0.8$, and $H_0 = 70 \text{ km s}^{-1} \text{ Mpc}^{-1}$. We use magnitudes in the AB system Oke & Gunn (1983).

2. SAMPLE AND DATA REDUCTION

2.1. Our ALMA Sample

The sample is drawn mainly from the literature (Capak et al. 2015; Willott et al. 2015; Pentericci et al. 2016; Smit et al. 2018; Carniani et al. 2018; Jones et al. 2017), selecting only star-forming galaxies at $z > 5$ whose [CII] lines have been detected (at signal-to-noise, $S/N \geq 5$) with ALMA. To obtain reliable results for representative galaxies in the early Universe, we limit our sample to galaxies with (i) star-formation rates (SFRs), $< 100 M_\odot \text{ yr}^{-1}$, (ii) no indication of AGN activity, (iii) no giant Ly α systems, such as Himiko (Ouchi et al. 2009) and CR7 (Matthee et al. 2015), (iv) no signs of gravitationally lensing, e.g. galaxies behind massive galaxy clusters, (v) [CII] line emission with a full width at half maximum (FWHM) broader than 80 km s^{-1} , and (vi) [CII] line detections that are reproduced in our own data reduction. We adopt (v) because the thermal noise fluctuation can produce peaky false source signals even with $S/N > 5$, when we examine the large volume data such as the ALMA 3D data cubes. Note that our sample does not include the tentative [CII] line detections reported in the ALMA blind line survey (Aravena et al. 2016; Hayatsu et al. 2017), because these tentative [CII] detections have not been spectroscopically confirmed. We identify 16 [CII] line sources that meet the above criteria in the literature. Table 1 summarises our sample and the references that describe the relevant ALMA observations.

In addition to the literature sample, we include new [CII] line detections of two star-forming galaxies, NB816-S-61269 (Ouchi et al. 2008; Fujimoto et al. 2016) and WMH13 (Willott et al. 2013) at $z = 5.688$ and 5.983 , respectively. In Figure 1, we present the velocity-integrated maps and the spectra for these two [CII] detections. In the velocity-integrated maps of NB816-S-61269 and WMH13, the [CII] line is detected with peak S/N levels of 6.0 and 5.2, respectively; rest-frame FIR dust continuum emission is not detected from either galaxy. The details of the ALMA observations for these additional sources are listed in Table 1.

From the literature and the additional samples, we obtain a total of 18 [CII] line sources. The 18 [CII] line sources have the spectroscopic redshifts determined by the [CII] lines ($z_{\text{[CII]}}$) and the absolute rest-frame UV magnitudes (M_{UV}) in the ranges of $z_{\text{[CII]}} = 5.153 - 7.142$ and $M_{\text{UV}} \simeq -22.8$ to -20.4 ($\text{SFR} \simeq 10 - 70 M_\odot/\text{yr}$). We summarize the physical properties of $z_{\text{[CII]}}$, M_{UV} , and the Ly α equivalent-width ($\text{EW}_{\text{Ly}\alpha}$) in Table 1.

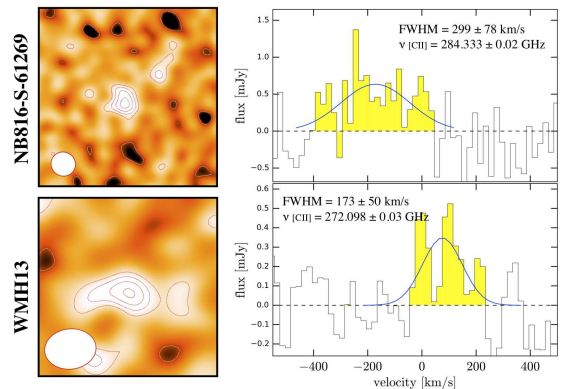


Figure 1. New [CII] line detections of NB816-S-61269 (top) and WMH13 (bottom). **Left:** Natural-weighted $4'' \times 4''$ field image of the velocity-integrated [CII] line intensity (moment zero) with contours at the -2σ (white), 2σ , 3σ , 4σ , and 5σ (red) levels. The ALMA synthesized beams are presented at the bottom left. **Right:** [CII] line spectra with an aperture diameter of $1''.2$. The solid curves denote the best-fit profile of the single Gaussian with the best-fit values of the FWHM and the frequency peak. The yellow shades present the integrated velocity ranges for the [CII] line intensity maps in the left panel.

2.2. ALMA Data

We reduce the ALMA data for our sample with the Common Astronomy Software Applications package (CASA; McMullin et al. 2007) in the standard manner with the scripts provided by the ALMA observatory. In this process, we carry out re-calibrations for the flux density and additional flagging for bad antennae if we find problems in the final images that shows striped patterns and/or significantly higher noise levels than expected. The continuum images and line cubes are produced by the CLEAN algorithm with the TCLEAN task with a pixel scale of $0''.01$. For the line cubes, the velocity channel width is re-binned to 20 km s^{-1} , where the velocity center is adjusted to the Ly α redshift. We do not CLEAN the line cubes because the [CII] line is faint in each 20 km s^{-1} channel. The CLEAN boxes were set at the peak pixel positions with $S/N \geq 5$ in the auto mode, and the CLEAN routines were proceeded down to the 3σ level. We list the standard deviation of the pixel values in a final natural-weighted image and a synthesized beam size for the continuum image in Table 1.

Note that the continuum is subtracted from the uv -data of the line cubes for 4 sources (Hz4, Hz6, Hz9, and WMH5) whose continuum emission is individually detected (Capak et al. 2015; Willott et al. 2015). The continuum level is estimated from the channels in the velocity range of $v > |2 \times \text{FWHM}|$ in the same baseband as the [CII] line emission.

2.3. HST Data

To study the rest-frame UV properties of our sample, we also use the HST Wide Field Camera 3 (WFC3) in F160W, $1.54 \mu\text{m}$ (H -band), images from the Hubble Legacy Archive, where we obtain final flat-field and flux-calibrated science products.

To correct the potential offsets of the HST astrome-

Table 1
Our ALMA Sample

Target	R.A. (J2000)	Dec. (J2000)	$z_{\text{[CII]}}$ ($z_{\text{Ly}\alpha}$)	M_{UV} (mag)	$\text{EW}_{\text{Ly}\alpha}$ (Å)	$\sigma_{\text{cont.}}$ † ($\mu\text{Jy/beam}$)	Beam ($'' \times ''$)	ALMA ID (6)	HST (7)	Ref. (8)
			(1)	(2)	(3)	(4)	(5)			
Literature										
WMH5	36.612542	−4.877333	6.069 (6.076)	−22.6	13.0	8	0.50×0.46	2013.1.00815.S 2015.1.00834.S	N	W15, J17 W15, J17
CLM1	37.012319	−4.271706	6.166 (6.176)	−22.6	50.0	18	0.52×0.45	2013.1.00815.S	N	W15
COS301855	150.125803	2.266613	6.854 (−)	−21.9	−2.9	27	1.08×0.74	2015.1.01111.S	Y	S18 (S14)
COS298703	150.124400	2.217294	6.808 (6.816)	−22.0	16.2	25	1.07×0.74	2015.1.01111.S	Y	S18 (S14)
NTTDF6345	181.403878	−7.756192	6.698 (6.701)	−21.5	15.0	20	1.25×0.97	2015.1.01105.S	N	P16
BDF2203	336.958267	−35.147529	6.122 (6.118)	−20.9	9.9	20	1.85×1.05	2016.1.01240.S	N	C18
COS13679	150.099014	2.343517	7.142 (7.145)	−21.4	15.0	18	0.85×0.85	2015.1.01105.S	N	P16
COS24108	150.197356	2.478931	6.623 (6.629)	−21.6	27.0	20	0.81×0.75	2015.1.01105.S	N	P16
Hz1	149.971828	2.118142	5.689 (5.690)	−22.0	5.3	27	0.75×0.52	2012.1.00523.S	Y	C15 (B17)
Hz2	150.517186	1.928936	5.670 (5.670)	−21.9	6.9	35	0.83×0.53	2012.1.00523.S	N	C15 (B17)
Hz3	150.039247	2.3371611	5.542 (5.546)	−21.7	−3.6	47	0.77×0.42	2012.1.00523.S	Y	C15 (B17)
Hz4	149.618760	2.051850	5.544 (5.310)	−22.3	10.2	64	0.89×0.51	2012.1.00523.S	Y	C15 (B17)
Hz6	150.089576	2.586324	5.293 (5.290)	−22.8	8.0	32	0.67×0.50	2012.1.00523.S	Y	C15 (B17)
Hz7	149.876925	2.134061	5.253 (5.250)	−21.8	9.8	35	0.47×0.38	2012.1.00523.S	Y	C15 (B17)
Hz8	150.016894	2.626631	5.153 (5.148)	−21.8	27.1	30	0.40×0.29	2012.1.00523.S	Y	C15 (B17)
Hz9	149.965404	2.378358	5.541 (5.548)	−21.9	14.4	43	0.64×0.54	2012.1.00523.S	Y	C15 (B17)
New Detection										
NB816−S−61269	34.438567	−5.493392	5.684 (5.688)	−20.4	93.3	22	0.45×0.42	2012.1.00602.S	N	F16
WMH13	149.985580	2.207528	5.985 (5.983)	−22.0	27.0	16	1.15×0.89	2013.1.00815.S	N	W15

Notes: (1) Spectroscopic redshift determined by the [CII] (Ly α) line emission. (2) Absolute magnitudes. (3) Rest-frame Ly α EW. (4) One sigma noise measured by the standard deviation of the pixel values in the continuum map before primary beam correction. (5) Synthesized beam size of our ALMA maps (weighting = "natural"). (6) ALMA project ID. (7) "Y" ("N") indicates the sources (not) included in the ALMA-HST sample. (8) ALMA (HST) data reference (W15: Willott et al. 2015, J17: Jones et al. 2017, S18: Smit et al. 2018, P16: Pentericci et al. 2016, C18: Carniani et al. 2018, S14: Smit et al. 2014, C15: Capak et al. 2015, B17: Barisic et al. 2017, F16: Fujimoto et al. 2016).

† Our additional flagging and difference in the imaging parameter setting may produce different values from the data references.

try (e.g., Rujopakarn et al. 2016; Dunlop et al. 2017), we calibrate the astrometry of the H -band maps with the Gaia Data Release 2 catalog (Gaia Collaboration et al. 2018). First, we identify bright objects in the H -band images with SEXTRACTOR version 2.5.0 (Bertin & Arnouts 1996). Second, we cross-match the bright H -band objects and the GAIA catalog. Finally, we evaluate offsets between the bright H -band object centers and the GAIA catalog positions. We find that the bright H -band object centers indeed have the offsets from the GAIA catalog in the range of $\sim 0''.1$ – $0''.3$. We correct the astrometry of each H -band map to match the GAIA catalog based on these offsets. We identify that 9 out of 18 sources in our sample have been observed with the HST/ H -band whose astrometry is successfully corrected with the above procedure. We refer to the 9 and the 18 sources as the "ALMA-HST" and "ALMA-ALL" samples, respectively. In Table 1, we summarize the HST data references and the sources included in the ALMA-HST sample.

Note that we confirm that the ALMA astrometry is well consistent with the GAIA catalog within a milli-arcsec scale via the bright quasars used as the phase calibrators in the ALMA observations. Thus, we do not carry out any astrometry corrections for our ALMA maps.

3. DATA ANALYSIS

3.1. 3D Position in ALMA Cube

To carry out stacking for the [CII] line and the rest-frame FIR continuum, we estimate source centroids for the 18 [CII] line sources in the ALMA 3-dimensional data cubes via the following six steps: (1) We create fidu-

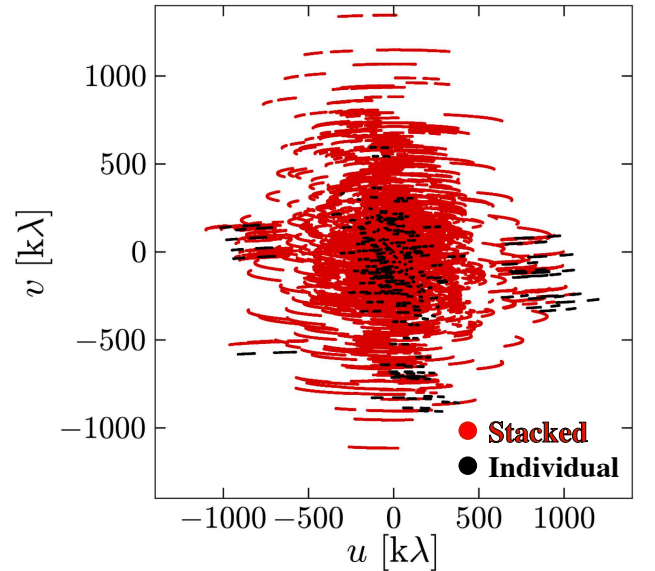


Figure 2. uv -visibility coverage for individual and stacked data. For the individual data, we present Hz3 data as an example. For the stacked data, the uv -visibility coverage less than 500 k λ is well sampled in circular symmetrically, which enables us to investigate the diffuse, extended structures.

cial [CII] velocity-integrated maps in the velocity range, ~ 100 – 900 km s^{-1} , that maximizes the S/N level of the [CII] line detection. (2) We measure fiducial positional

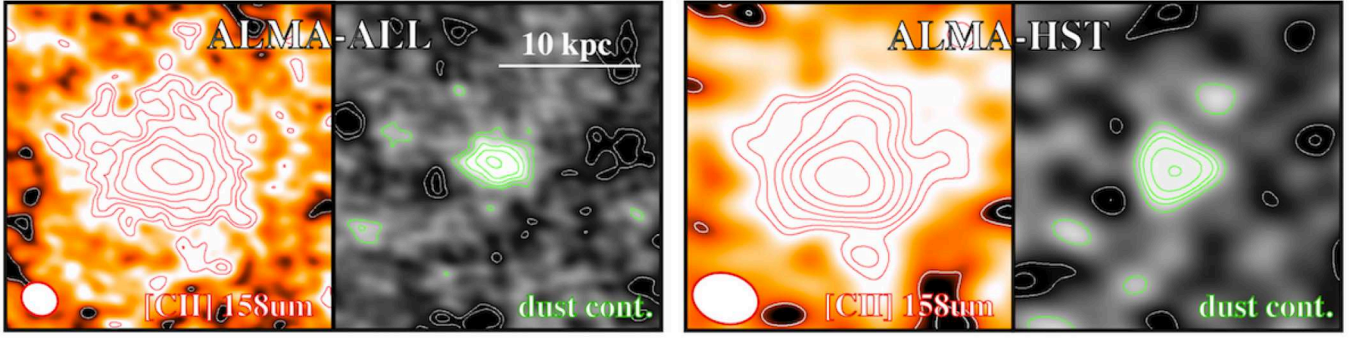


Figure 3. Natural-weighted $4'' \times 4''$ field image after the visibility-based stacking of the [CII] line and the dust continuum for the ALMA-ALL (left) and ALMA-HST (right) samples. The red and green contours denote the $2, 2\sqrt{2}, 4, \dots \times \sigma$ levels of the [CII] line and the dust continuum emission, while the white contours indicate the -2σ and $-2\sqrt{2}\sigma$ levels. The synthesized beams are presented at the bottom left in each panel.

centroids based on the peak pixel positions (pixel scale = $0''.01$) in the fiducial [CII] velocity-integrated maps, having smoothed spatially with a uv -taper of $0''.6$. (3) We produce [CII] spectra with an aperture diameter of $1''.2$ at the fiducial source centroids. (4) We obtain the peak frequencies and FWHMs of the [CII] line emission by fitting a single Gaussian to the [CII] spectra. (5) We re-create velocity-integrated maps with velocity ranges of $2 \times$ the FWHM. (6) We measure final positional centroids in the new velocity-integrated map in the same manner as step (2). Note that we use the smoothed map (via the uv -taper) instead of the naturally-weighted map in steps (2) and (6) because Monte-Carlo simulations in the uv -visibility plane show that smoothed maps have lower uncertainties in the positional measurements than the intrinsic maps (Fujimoto et al. 2018). We list the final positional centroids and redshifts in Table 1.

3.2. ALMA Visibility-based Stacking

We carry out visibility-based stacking for our ALMA data via the following procedure. First, we split the visibility data into the [CII] line and the rest-frame FIR continuum datasets. For the [CII] line dataset, we extract the visibility data with the [CII] line channels across a velocity range of 100 km s^{-1} ($= \pm 50 \text{ km s}^{-1}$), where the velocity centre is the [CII] frequency peak (the 3D position in our ALMA cubes). We do not adopt a wider velocity range because of the potential contamination of the close companions (Jones et al. 2017; Carniani et al. 2018). For the rest-frame FIR continuum dataset, we produce the visibility data whose [CII] line channels in a velocity range of $2 \times \text{FWHM}$ are fully removed. Second, we shift the coordinate of the visibility datasets by re-writing the source centre as "00:00:00.00 00:00:00.0" with STACKER (Lindroos et al. 2015). Third, we combine the visibility datasets with the CONCAT task. Fourth, we re-calculate the data weights for the combined visibility datasets with the STATWT task, based on the scatter of visibilities, which includes the effects of integration time, channel width and system temperature.

Figure 2 indicates the uv -visibility coverage after the visibility-based stacking for the ALMA datasets of the

ALMA-ALL sample. For comparison, the uv -visibility coverage for an individual dataset, before stacking, is also plotted. In the stacked data, the uv -visibility coverage is well sampled, especially for the short baselines, $< 500 \text{ k}\lambda$, which is important to recover the flux density from diffuse, extended structures.

In Figure 3, we show the natural-weighted images of the [CII] line and dust continuum after the visibility-based stacking for the ALMA-ALL (ALMA-HST) sample, where the standard deviation of the pixel values in the dust continuum image achieves 4.1 (8.3) $\mu\text{Jy/beam}$ with the synthesized beam size of $0''.43 \times 0''.36$ ($0''.74 \times 0''.58$). The peak pixel signal-to-noise (S/N) ratio shows 21σ (20σ) and 10σ (8σ) significance levels for the [CII] line and dust continuum, respectively, for the ALMA-ALL (ALMA-HST) sample. The spatially resolved [CII] line emission in the ALMA-ALL sample is detected at the 9.3σ level in the aperture radius of 10 kpc even after masking the emission in a central area up to $2 \times \text{FWHM}$ of the ALMA synthesized beam, based on the random-aperture method. Because the extended structure is difficult to be modeled by the CLEAN algorithm perfectly, we use the dirty images for both the [CII] line and the rest-frame FIR continuum in the following analyses.

In Figure 4, we present the radial surface brightness profile of the stacked [CII] line, and summarize various tests for the extended [CII] line structure. First, we compare our stacking and individual results. In the left panel of Figure 4, we show the individual results for several [CII] line sources whose lines are detected at high S/N, with an ALMA beam size of $\gtrsim 0''.8$ to recover the diffuse, extended structures. We find that the stacked results are consistent with the individual results within the scatter, suggesting that our ALMA stacking result provides a faithful representative of the 18 [CII] line sources. Second, we remove the sources that are I) taken with the lowest resolutions (BDF2203, NTTDF6345, and WMH13), and II) reported to have companions (WMH5, Hz2, Hz6, and Hz8; Jones et al. 2017; Carniani et al. 2018), and obtain a newly stacked data. In the middle panel of Figure 4, we present the radial profiles of the [CII] line emission in the newly stacked data. We

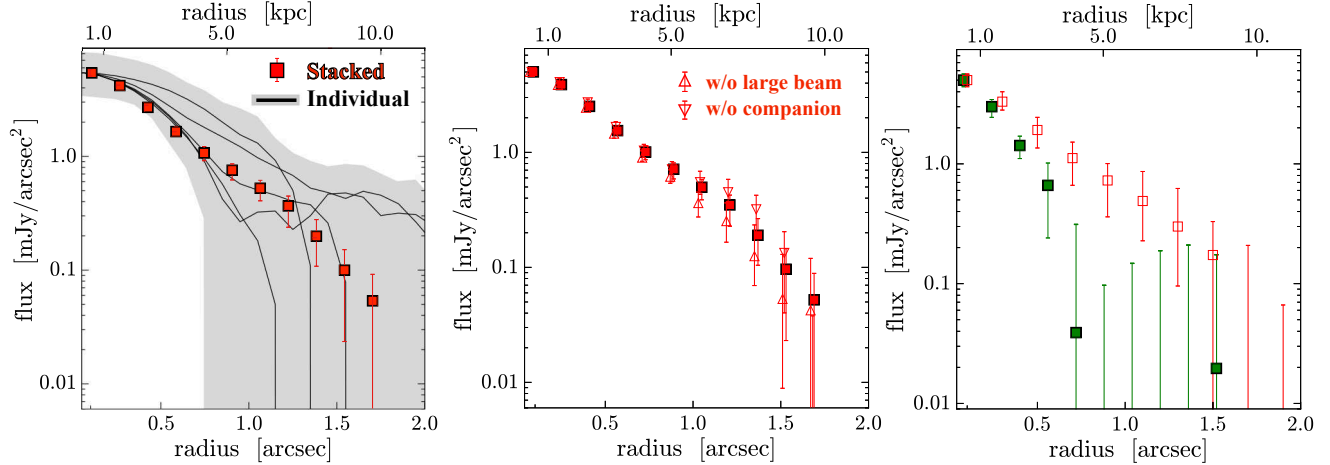


Figure 4. Radial surface brightness profile of the [C II] line (red filled squares) and dust-continuum (green filled squares) emission for the ALMA-ALL sample. **Left:** The black solid curves denote the individual results from five [C II] line sources whose [C II] lines are detected with high S/N levels and with the ALMA beam sizes of $\gtrsim 0''.8$ to recover the diffuse, extended structures. The gray shades indicate the error range of the individual results. **Middle:** The re-stacked results without the [C II] line sources that are I) taken with the lowest resolutions (BDF2203, NTTDF6345, and WMH13; upward triangle), and II) reported to have companions (WMH5, Hz2, Hz6, and Hz8; downward triangle), respectively. **Right:** The radial profile of the [C II] line in the noise-enhanced map (open square) whose peak S/N ratio is reduced down to the level comparable to the dust continuum map. All radial profiles are normalized to the peak value of the [C II] line.

find that the newly stacked [C II] line profiles reproduce the extended structures that are well consistent with the original stacking result in the ALMA-ALL sample. This indicates that the extended [C II] line structure is not caused either by the bias to the low-resolution data or the contamination of the companions. Third, we compare the structures of the [C II] line and the dust continuum in the same significance level. We produce a random noise map smoothed by the ALMA beam, and combine the noise and the stacked [C II] line maps. Changing the noise levels, we obtain the noise-enhanced [C II] line map whose peak S/N ratio becomes comparable to the dust continuum one. We create the 50 noise-enhanced [C II] line maps. In the right panel of Figure 4, we show the 16–84th percentile of the [C II] radial profile in the noise-enhanced maps. We find that the [C II] line profile still exceeds more than the dust continuum in these noise-enhanced maps, showing that the different structures between the [C II] line and the dust continuum are not mimicked by the difference in the dynamic range.

3.3. *HST/H-band Stacking*

We have performed image-based stacking for the ALMA-HST sample, exploiting their deep archival *HST* *H*-band imaging. Before stacking, we carry out the following procedure: 1) We cut out $8'' \times 8''$ stamps from the *H*-band images, around the [C II] line sources, and set the pixel scale to $0''.01$, which corresponds to our ALMA images. 2) We identify low-redshift contaminants within $2''.0$ from the [C II] sources, by cross-matching the [C II] line source positions with photometric redshift catalogs (Ilbert et al. 2013; Skelton et al. 2014). 3) We remove the low-redshift contaminants from the *H*-band images by fitting Sérsic profiles (Sérsic 1963) with GALFIT (Peng et al. 2010). We then proceed to generate an average stack, weighted by the noise levels of the ALMA

images of the [C II] line source. This is because the visibility-based stacking for our ALMA data is weighted by the visibility scatter, which generally corresponded to the noise levels on the ALMA images.

In panel (f) of Figure 5, we show the stacked *H*-band image for the ALMA-HST sample. In the *HST* stacking, we adopted stacking centroids defined by the peak positions of the *H*-band images, smoothed with the *uv*-tapered ALMA beams in a consistent manner with the [C II] line stacking.

To directly compare the size and morphology of the *HST* and ALMA images, we make a mock *H*-band image whose PSF is matched to the ALMA beam of the ALMA-HST sample. We use GALFIT to obtain a kernel with which the *H*-band PSF can be converted to the ALMA beam. For the kernel, we assume a sum of three independent Sérsic profiles whose positions are fixed at the centre. In Figure 5, we present a schematic overview of converting the *H*-band PSF to the ALMA beam. Within a radius of $1''.0$ on the residual map, we find that the errors between the modeled and the real ALMA beams are less than $\sim 1.8\%$, showing that the best-fit kernel reproduces the ALMA beams well from the *H*-band PSF. By applying the convolution with the best-fit kernel to the stacked *H*-band image, we finally obtain the mock *H*-band image whose PSF is almost the same as the stacked ALMA image.

4. RESULTS

4.1. *Discovery of [C II] Halo*

Figure 6 presents the radial surface brightness profiles of the [C II] line, rest-frame FIR, and UV continuum, derived from the stacking results for the ALMA-HST (circles) and ALMA-ALL (squares) samples. For fair comparison, the ALMA-HST results are obtained by re-performing the ALMA visibility-based stacking with the

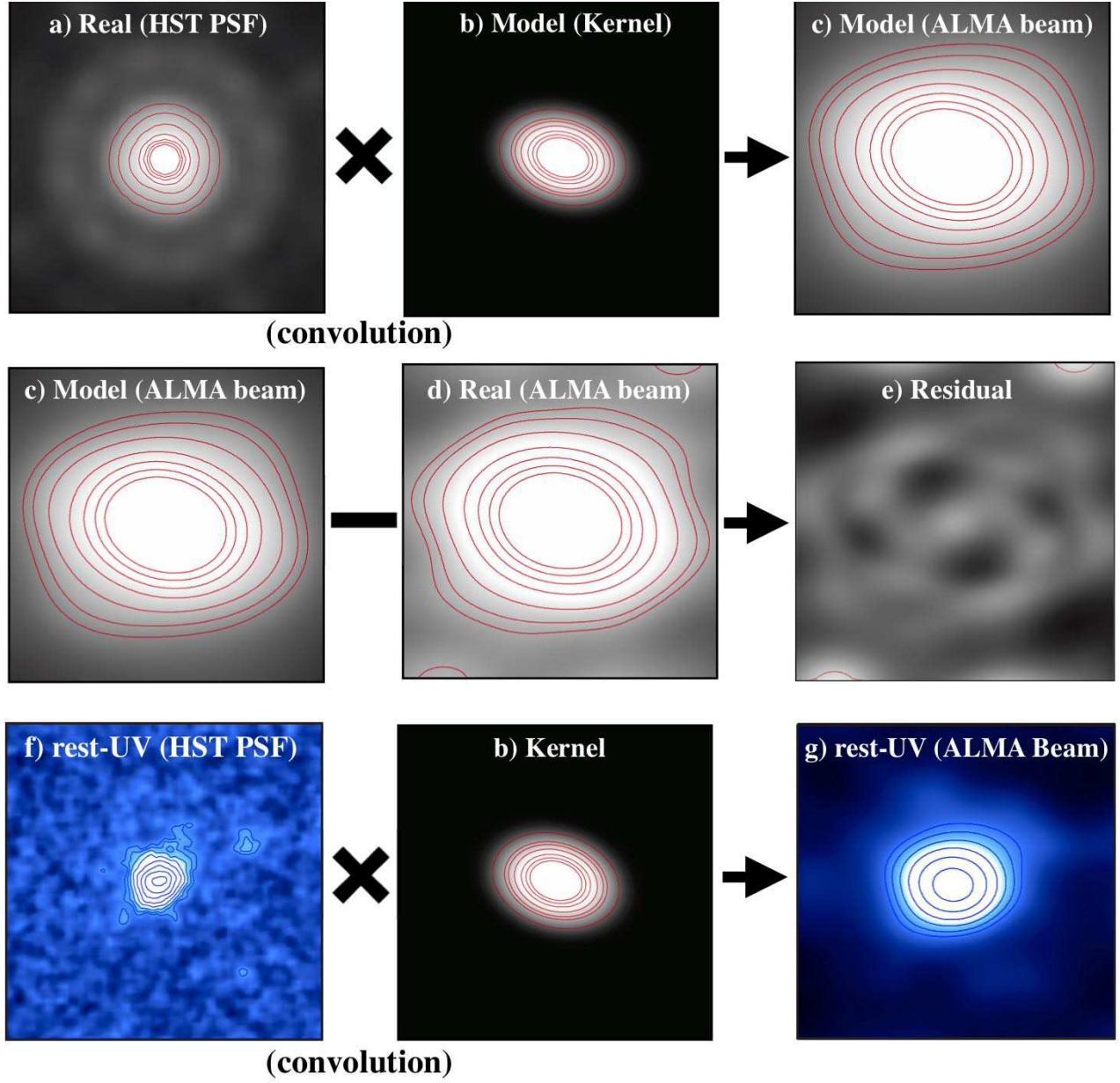


Figure 5. Schematic overview to obtain the mock HST/H-band image whose spatial resolution is matched to the stacked ALMA image for the ALMA-HST sample: a) HST/H-band PSF, b) the best-fit kernel composed by three Sérsic profiles obtained with GALFIT, c) the best-fit ALMA beam model obtained with GALFIT, d) the synthesized beam in the stacked ALMA image for the ALMA-HST sample, e) the residual between c) and d), f) the stacked HST/H-band image for the ALMA-HST sample, and g) the stacked HST/H-band image obtained by convolving f) with b). The red contours present 3%, 5%, 10%, 20%, 30%, 40%, and 50% of the PSF or beam response. The blue contours denote the $2, 2\sqrt{2}, 4, \dots \times \sigma$ levels of the rest-frame UV continuum emission. The cutout sizes are $2'' \times 2''$ and $4'' \times 4''$ for the panels of a)–e) and f)–g), respectively.

HST/H-band peak positions, while the ALMA-ALL results are not due to the lack of the HST/H-band images.

In Figure 6, the ALMA-ALL and ALMA-HST results show a good agreement in both profiles of the [C II] line and the rest-FIR continuum. We find that the radial profile of the [C II] line emission is extended up to a radius of ~ 10 kpc which contrasts the rest-frame UV and FIR continuum. Because the typical effective radius of the normal star-forming galaxies at $z \sim 6$ is estimated to be less than 1 kpc (e.g., Shibuya et al. 2015), the ~ 10 -kpc scale structure at this epoch corresponds to the circum-

galactic medium (CGM) surrounding the galaxies. These results suggest that the [C II] line emission is produced in the wide CGM areas even without stellar continuum. We discuss the physical origin of the [C II] halo in Section 5.

We also find that the profiles of the rest-frame FIR and UV continuum are consistent within the 1σ errors. Note that the rest-frame FIR continuum is likely to follow the ALMA beam, while the rest-frame UV continuum is slightly resolved with the ALMA beam. This suggests that the intrinsic size of the rest-frame FIR continuum

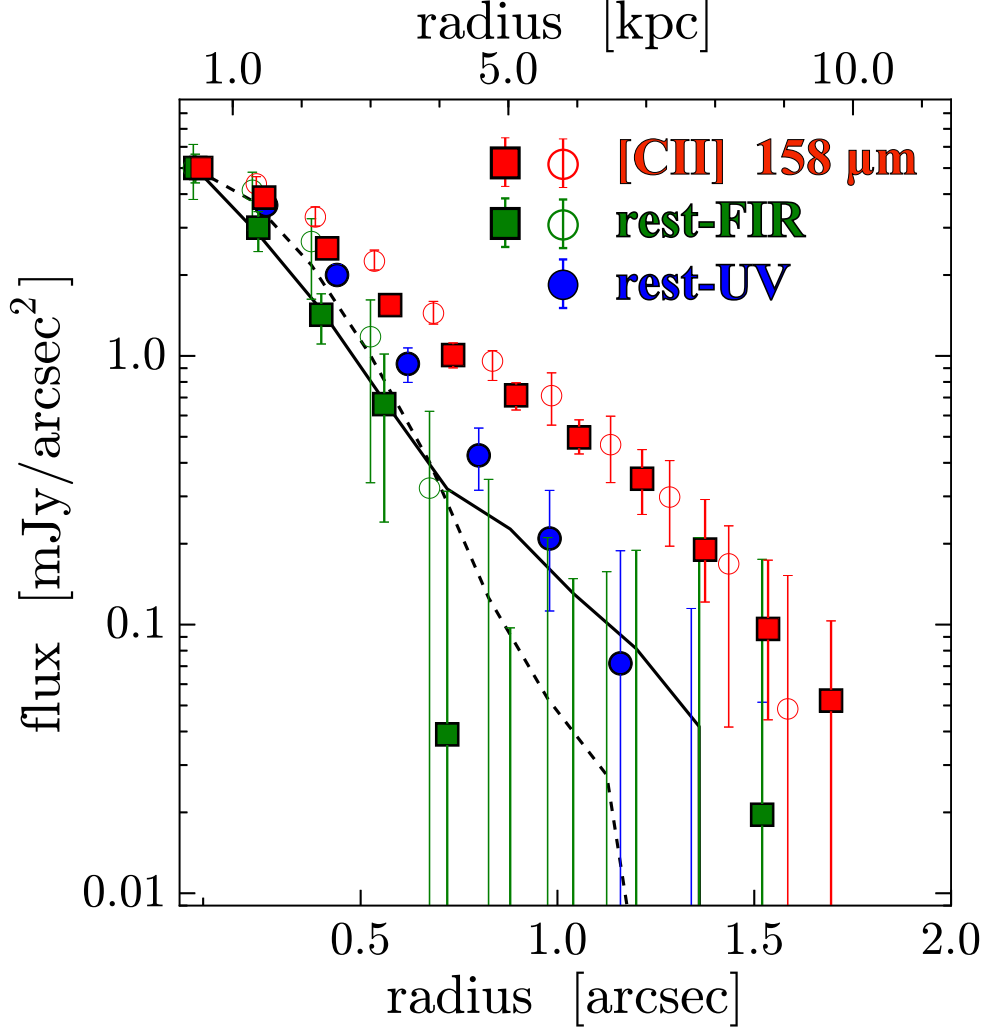


Figure 6. Radial surface brightness profiles for the ALMA-HST (circles) and ALMA-ALL (squares) samples. The radial values are estimated by the median of each annulus. The red, green, and blue symbols denote the [CII] line, rest-frame FIR, and rest-frame UV continuum emission. The rest-frame UV continuum profile is directly derived from the mock HST/*H*-band image whose resolution is matched to that of the ALMA image. The black dashed and solid curves denote the ALMA synthesized beams in the stacked images of the ALMA-HST and ALMA-ALL samples, respectively. All radial profiles are normalized to the peak value of the [CII] line. The green and red symbols are slightly shifted along the x -axis for clarity.

is smaller than that of the rest-frame UV continuum, which is consistent with the recent ALMA results of the compact rest-frame FIR size more than the rest-frame UV and optical sizes among the star-forming galaxies at $z \sim 2 - 4$ (e.g., Simpson et al. 2015; Ikarashi et al. 2015; Hodge et al. 2016; Fujimoto et al. 2017, 2018).

4.2. Effect of [CII]-UV offset

Recent studies report a possibility that [CII]-line emitting regions are physically offset from the rest-frame UV ones (e.g., Maiolino et al. 2015). To evaluate the potential effect from the [CII]-UV offsets in our results, we perform the ALMA and HST stacking for the ALMA-HST sample by adopting two different stacking centers: HST/*H*-band and ALMA [CII] line peak positions, and compare the radial profiles from these stacking results.

In Figure 7, the circle and cross symbols represent the stacking results derived with the common stacking centers of the HST/*H*-band continuum and ALMA [CII] line

peak positions, respectively. We find that the [CII] line profile is extended more than both the rest-frame FIR and UV continuum profiles in any cases. This suggests that the [CII] line originates from much wider regions than the continuum emission at rest-frame FIR and UV wavelengths, and clearly shows that the extended structure of the [CII] line is not caused by the [CII]-UV offsets.

4.3. Radial ratio of $L_{\text{[CII]}}$ to total SFR

To test whether the extended [CII] line structure is caused by satellite galaxies, we investigate radial values of the [CII] line luminosity $L_{\text{[CII]}}$ at a given SFR derived from the rest-frame FIR and UV continuum. Because the ALMA-ALL and ALMA-HST results are consistent with each other (Figure 6), we adopt the rest-frame UV results from the ALMA-HST sample, while the [CII] line and rest-frame FIR continuum results from the ALMA-ALL

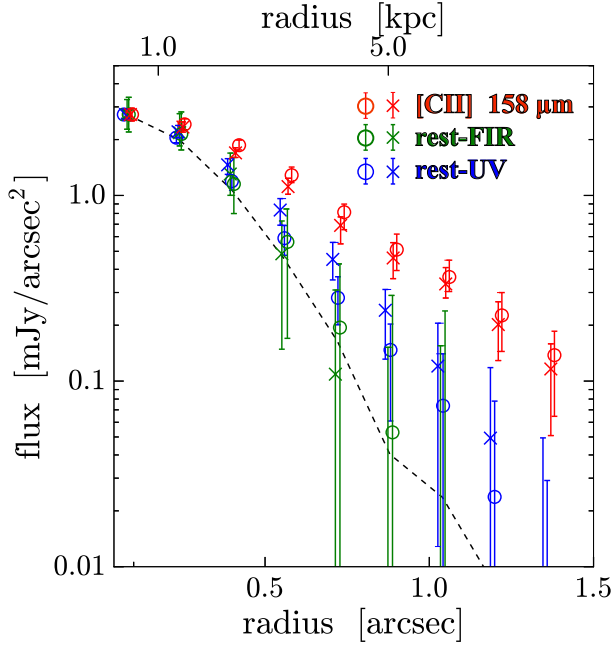


Figure 7. Radial surface brightness profiles for the ALMA-HST sample derived with different stacking centers. The red, green, and blue symbols denote the [CII] line, rest-frame FIR, and rest-frame UV continuum emission. The color crosses and circles are the stacking results based on the stacking centers of the [CII] line and the HST/*H*-band peak positions, respectively. The rest-frame UV continuum profile is directly derived from the mock HST/*H*-band image whose resolution is matched to the ALMA image. The black solid curve denotes the ALMA synthesized beam. All radial profiles are normalized to the peak value of the [CII] line. The green and red symbols are slightly shifted along the *x*-axis for clarity.

sample to reduce the errors in the following estimates.

We first estimate the radial surface density value of $L_{\text{[CII]}}$ ($\Sigma L_{\text{[CII]}}$). For our sources, the weighted-average source redshift and FWHM of the [CII] line width are estimated to be $z = 6.01$ and 270 km s^{-1} , respectively. Since the velocity-integrated width is 100 km s^{-1} in the stacked [CII] line map, we correct the velocity-integrated value in the range from 100 km s^{-1} to 270 km s^{-1} , assuming a single Gaussian line profile, to recover the total $L_{\text{[CII]}}$ value. We second evaluate the radial surface density value of SFR (ΣSFR). We derive the obscured (SFR_{IR}), un-obscured (SFR_{UV}), and total SFR ($\text{SFR}_{\text{total}}$) with the equations in Murphy et al. (2011) of

$$\text{SFR}_{\text{IR}} [M_{\odot} \text{ yr}^{-1}] = 3.88 \times 10^{-10} L_{\text{IR}} [\text{erg s}^{-1}], \quad (1)$$

$$\text{SFR}_{\text{UV}} [M_{\odot} \text{ yr}^{-1}] = 4.42 \times 10^{-10} L_{\text{UV}} [\text{erg s}^{-1}], \quad (2)$$

$$\text{SFR}_{\text{total}} = \text{SFR}_{\text{IR}} + \text{SFR}_{\text{UV}}, \quad (3)$$

where L_{IR} is the integrated IR flux density estimated by a typical modified blackbody whose spectral index β_d and dust temperature T_d are $\beta_d = 1.8$ (Planck Collaboration et al. 2011) and $T_d = 35 \text{ K}$ (Coppin et al. 2008), and L_{UV} is the rest-frame UV luminosity at $0.16 \mu\text{m}$ with the HST *H*-band. Finally, we divide the radial $\Sigma L_{\text{[CII]}}$ values by the radial ΣSFR values and obtain the radial ratio of $L_{\text{[CII]}}/\text{SFR}_{\text{total}}$.

In Figure 8, we show $\Sigma L_{\text{[CII]}}$, $\Sigma \text{SFR}_{\text{total}}$ (middle panel), and ratio of $L_{\text{[CII]}}/\text{SFR}_{\text{total}}$ (right panel) as a

function of radius derived from our stacking results. For comparison, the right panel of Figure 8 also presents possible $L_{\text{[CII]}}/\text{SFR}_{\text{total}}$ ratios of the potential satellite galaxies. The possible ratios are estimated from the $L_{\text{[CII]}}-\text{SFR}_{\text{total}}$ relations in local star-forming and dwarf galaxies (De Looze et al. 2014) in the following steps. First, we calculate the $\text{SFR}_{\text{total}}$ values for the potential satellite galaxies: at a given radius, the radial $\Sigma \text{SFR}_{\text{total}}$ value is derived in the middle panel, where we obtain the $\text{SFR}_{\text{total}}$ value for the potential satellite galaxies by assuming an average effective radius of 0.7 kpc in $z \sim 6$ normal star-forming galaxies (Shibuya et al. 2015). Second, with these $\text{SFR}_{\text{total}}$ values, we estimate the $L_{\text{[CII]}}$ values via the $L_{\text{[CII]}}-\text{SFR}_{\text{total}}$ relations. Finally, we evaluate the possible range of the $L_{\text{[CII]}}/\text{SFR}_{\text{total}}$ ratios based on the 1σ errors of the relations.

In the right panel of Figure 8, we find that the ratios in our stacking results become higher towards the halo areas. Moreover, the high ratios of our stacking results cannot be explained either by star-forming or dwarf galaxies at the radius of $\gtrsim 4 \text{ kpc}$. These results indicate that the [CII] halo is not formed by the satellite galaxies, but other mechanisms whose contribution is increased as a function of the distance from the galaxy centre. We discuss the possible mechanisms of the [CII] halo in Section 5.

4.4. Scale Length of [CII] Halo

We characterize the detail radial surface brightness profile of the [CII] line emission by two-component fitting with GALFIT. Here we assume the two components as the central and the halo components.

For the central component, we adopt the Sérsic profile whose parameters are estimated from the rest-frame UV profile in the stacked HST/*H*-band image (Figure 5 f). We obtain the best-fit effective radius r_e and the Sérsic index n of $r_e = 1.1 \pm 0.1$ and $n = 1.2 \pm 0.01$ that are consistent with the average values estimated from the normal star-forming galaxies at $z \sim 6$ (Shibuya et al. 2015). For the halo component, we utilize the exponential profile. The exponential profile has been used for scale-length measurements of the Ly α halo which is universally identified around the high-*z* star-forming galaxies (e.g., Steidel et al. 2011; Matsuda et al. 2012; Momose et al. 2016; Leclercq et al. 2017). The exponential profile is described as $C_n \exp(-r/r_n)$ where C_n is a constant and r_n is the scale length. We fix the central positions of both central and halo components to obtain a stable result.

Figure 9 presents the best-fit results with the Sérsic+exponential profiles for the [CII] line emission. We obtain the best-fit scale-length values of $r_n = 3.3 \pm 0.1 \text{ kpc}$. This corresponds to the best-fit effective radius of $r_e = 5.6 \pm 0.1 \text{ kpc}$, showing that the [CII] halo is extended ~ 5 times more than the stellar continuum in the central galactic component.

In Figure 9, we compare the radial surface brightness profiles of the [CII] with the Ly α halos universally identified in the normal star-forming galaxies at $z \sim 3-6$ (e.g., Momose et al. 2016; Leclercq et al. 2017). For the [CII] line emission, we adopt the result from the ALMA-ALL sample due to the high significance detection. For the Ly α line emission, we use the recent results with the deep MUSE data for the high-*z* LAEs of Leclercq et al.

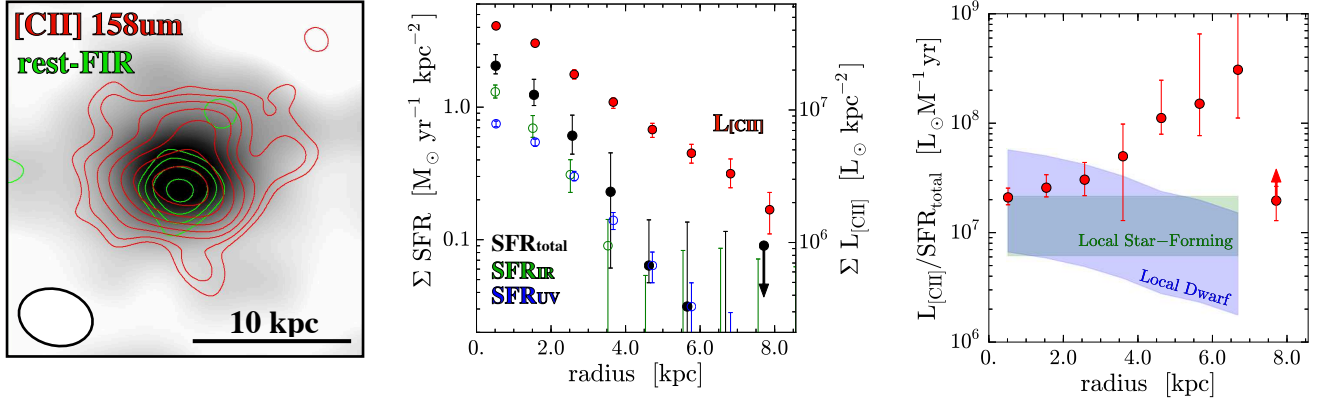


Figure 8. **Left:** Rest-frame UV emission of the ALMA-HST sample in the HST/*H*-band $4'' \times 4''$ image whose resolution is matched to the ALMA image. The red and green contours denote the 2, $2\sqrt{2}$, 4, ... $\times \sigma$ levels of the [CII] line and the dust continuum emission, respectively. The ALMA synthesized beam is presented at the bottom left. **Middle:** Radial profiles of ΣSFR (left axis) and $\Sigma L_{[\text{CII}]}$ (right axis). The blue, green, and black circles indicate $\Sigma \text{SFR}_{\text{UV}}$, $\Sigma \text{SFR}_{\text{IR}}$, and $\Sigma \text{SFR}_{\text{total}}$, respectively, based on Equations (1)–(3). The red circles denote $\Sigma L_{[\text{CII}]}$ normalized to ΣSFR with the ratio of $L_{[\text{CII}]} / \text{SFR}_{\text{total}} = 10^7 [L_{\odot} \text{M}_{\odot}^{-1} \text{yr}]$ that is the average value in the local star-forming galaxies (De Looze et al. 2014). **Right:** Radial ratio of $L_{[\text{CII}]} / \text{SFR}_{\text{total}}$ for our ALMA sources (red circles). The green and blue shades are obtained from the spatially integrated $L_{[\text{CII}]} - \text{SFR}_{\text{total}}$ relations (De Looze et al. 2014) for the local star-forming and dwarf galaxies, respectively (see text for details). At the radius of > 7 kpc, the $\text{SFR}_{\text{total}}$ value becomes negative due to the noise fluctuations on the low surface brightnesses of the rest-frame UV and FIR continuum emission, where we evaluate the lower limit of the ratio by using the upper limit of $\text{SFR}_{\text{total}}$.

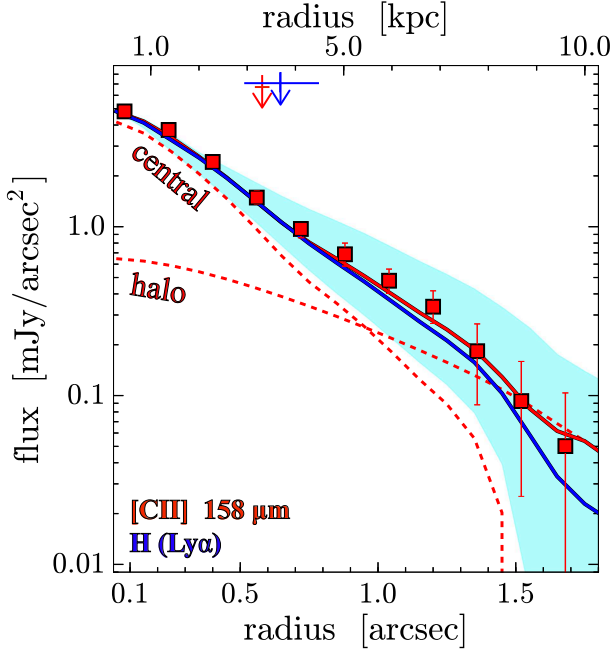


Figure 9. Two-component Sérsic+exponential profile fitting for the [CII] line, averaged over 18 galaxies. The red-dashed curves represent the best-fit results of the central stellar continuum and outer halo components, while the solid red curve denotes the sum of the best-fit two-component results. The solid blue curve and the shaded region indicate the median and the 16–84th percentile of the radial surface brightness profile of the Ly-alpha lines in a recent control sample from MUSE (Leclercq et al. 2017). For the Ly-alpha line, we convolve the best-fit results of the Sérsic+exponential profiles with the ALMA beam. The red and blue arrows with error bars show the best-fit scale lengths of the [CII] and the Ly-alpha halo components, respectively.

(2017), where the authors estimate the best-fit radial surface brightness profiles by fitting the two component Sérsic+exponential profile. We select the best-fit results of 6 LAEs at $z > 5$ with $M_{\text{UV}} \lesssim -21$ mag and $\text{EW}_{\text{Ly}\alpha} < 100 \text{ \AA}$ that are consistent with the parameter space of our sample (Table 1). We find that the radial surface brightness profile of the [CII] line emission is comparable to that of the Ly-alpha line emission. The median r_n value for the 6 LAEs is estimated to be 3.8 ± 1.7 kpc that is consistent with our best estimate of 3.3 ± 0.1 kpc. These results may imply that the physical origin of the extended [CII] line emission is related to the Ly-alpha halo.

4.5. [CII] Stacked Spectrum

We also perform the stacking for the [CII]-line spectra of the ALMA-ALL sample to test whether the our ALMA sample has a broad wing feature which is a good probe for the on-going outflow activities. For the stacking procedure, we adopt the same manner as previous ALMA studies (Decarli et al. 2018; Bischetti et al. 2018). Here we adopt a relatively small aperture diameter of $0''.4$ for the individual spectra to reduce the contamination of the close companions (Jones et al. 2017; Carniani et al. 2018).

In Figure 10, we show the stacked [CII]-line spectrum with the best-fit two Gaussian component model: the combination of the core and broad components whose velocity centers are fixed at 0 km/s for the stable results. The best-fit FWHMs are estimated to be 296 ± 40 km/s and 799 ± 654 km/s for the core and broad components, respectively. In the velocity range of $\pm 400 - 800$ km/s, the velocity-integrated intensity is tentatively detected at the 3.2σ level. These results may suggest the existence of the broad wing feature that is originated by the on-going outflow activities in our ALMA sample.

Note that there are other possibilities that produce the

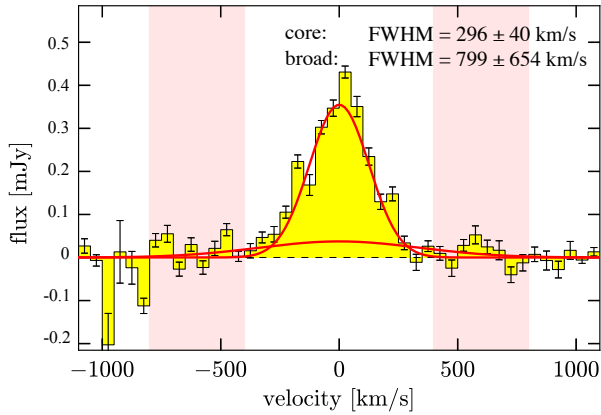


Figure 10. ALMA [C II]-line spectrum averaged over the ALMA-ALL sample. The spectrum is derived with the aperture diameter of $0''.4$. The red curves denote the best-fit two (= core + broad) Gaussian component model. The shade regions indicate the velocity ranges in which the velocity-integrated intensity is tentatively detected at the 3.2σ level.

broad wing feature. One possibility is that the contamination of the satellite galaxies. The [C II] line emission from the individual satellite galaxies can be smoothed in the stacking procedure for the 18 galaxies, which may be identified as the broad wing feature. Another possibility is that the faint continuum emission is mistakenly identified as the broad wing feature. Although we have performed the continuum subtraction for the [C II] line data cubes of the 4 galaxies whose continuum emission is individually detected, it is possible that the faint continuum emission from the rest of the 14 (= 18 - 4) galaxies appears in the deeply stacked spectrum. We thus do not give any conclusions with this stacked spectrum results.

4.6. Comparison with Model

We compare our observational results with a state-of-the-art zoom-in simulation of a star-forming galaxy, Althæa (Pallottini et al. 2017a,b; Behrens et al. 2018), with a halo mass of $M_{\text{halo}} \sim 10^{12} M_{\odot}$ at $z \sim 6$. Note that our sample is characterized by the average M_{UV} value of ~ -22 mag (Table 1) which corresponds to $M_{\text{halo}} \approx 10^{12} M_{\odot}$ from the $M_{\text{UV}}-M_{\text{halo}}$ relation (Harikane et al. 2018). Althæa therefore provides a reasonably representative context in which to examine our observational results.

In the zoom-in simulation, the hydrodynamical and dust radiative transfer (RT) simulations are combined, which provides realistic predictions for the spatial distribution of the [C II] line as well as the rest-frame FIR and UV continuum emission, with a spatial resolution of 30 pc. The hydrodynamical and the dust RT simulations are fully described in previous studies (Pallottini et al. 2017a,b; Behrens et al. 2018). Note that the dust RT is calculated as a post-processing step on snapshots of the hydrodynamical simulation. The [C II] line emission is computed in post-processing (Vallini et al. 2015) by adopting the photoionisation code, CLOUDY (Ferland et al. 2017). In these processes, CMB suppression (da Cunha et al. 2013; Zhang et al. 2016; Pallottini et al. 2015) is included in the calculation.

The left panel of Figure 11 presents a color compos-

ite of the [C II] line, rest-frame UV, and FIR continuum emission of Althæa at $z = 6.0$ in the zoom-in simulation. The surface brightness morphology of the [C II] line emission clearly shows the extended structure over the 10-kpc scale with surrounding satellite clumps and filamentary structures. The picture of the extended [C II] halo around the central galaxies is fully consistent with the observational results.

To quantitatively compare the zoom-in simulation to our observational results, we carry out the stacking for the zoom-in simulation results of the [C II] line, the rest-frame FIR and the rest-frame UV continuum in the same manner as the observations. First, we make 12 independent snapshots of Althæa at different redshifts within $6.0 \leq z \leq 7.2$. In each snapshot, we calculate the surface brightness from face-on and three random angles, where the [C II] line emissivity is calculated within 100 km s^{-1} of the velocity center to match the visibility-based stacking procedure for the ALMA data. From the first step, we obtain 48 (= 12×4) snapshots of Althæa at different evolutionary stages and angles. Second, we randomly select 9 from the 48 snapshots – the same sample size used when stacking with the ALMA-HST sample. Third, we determine the stacking centers from the peak positions of the rest-frame UV continuum images. Here we measure the peak positions on the 9 snapshots smoothed by the ALMA beams with uv tapers of $0''.6$ after adding Gaussian random noise, because the same uncertainties as the observations should be included in the determination of the stacking centers. Finally, we perform the stacking of the intrinsic images, and smooth the stacked images with the ALMA beam.

In the right panel of Figure 11, we show the radial surface brightness profiles estimated from the zoom-in simulation after the above stacking procedure. For comparison, we also plot the observational results obtained in Section 4. We find that the zoom-in simulation results well reproduce the following two observational trends: the radial surface brightness profile of I) the [C II] line is more extended than that of the rest-frame FIR and UV continuum; and II) the rest-frame UV continuum follows that of the rest-frame FIR continuum. However, we also find that the [C II] line emission in the zoom-in simulation results is insufficient to the extended [C II] halo component. This indicates that the existence of the [C II] halo challenges current galaxy evolution models.

5. DISCUSSION

In Section 4, we find that the [C II] line emission is extended up to ~ 10 -kpc scale surrounding around the normal star-forming galaxies at $z = 5 - 7$ and is potentially related to the Ly α halo. In contrast to the previous reports of the 10-kpc-scale carbon reservoirs around rare, massive galaxies, such as dusty starbursts and quasars at $z \sim 2-6$ (e.g., Ivison et al. 2011; Falgarone et al. 2017; George et al. 2014; Maiolino et al. 2012), our results indicates that the cold carbon gas halos universally exists even around early normal galaxies.

Theoretical studies suggest following five physical origins of the extended [C II] line emission with the potential association of the Ly α halo: A) satellite galaxies; B) circum-galactic (CG) photodissociation region (PDR); C) photoionization; D) cold streams; and E) outflow. These five possible origins are illustrated in Figure 12.

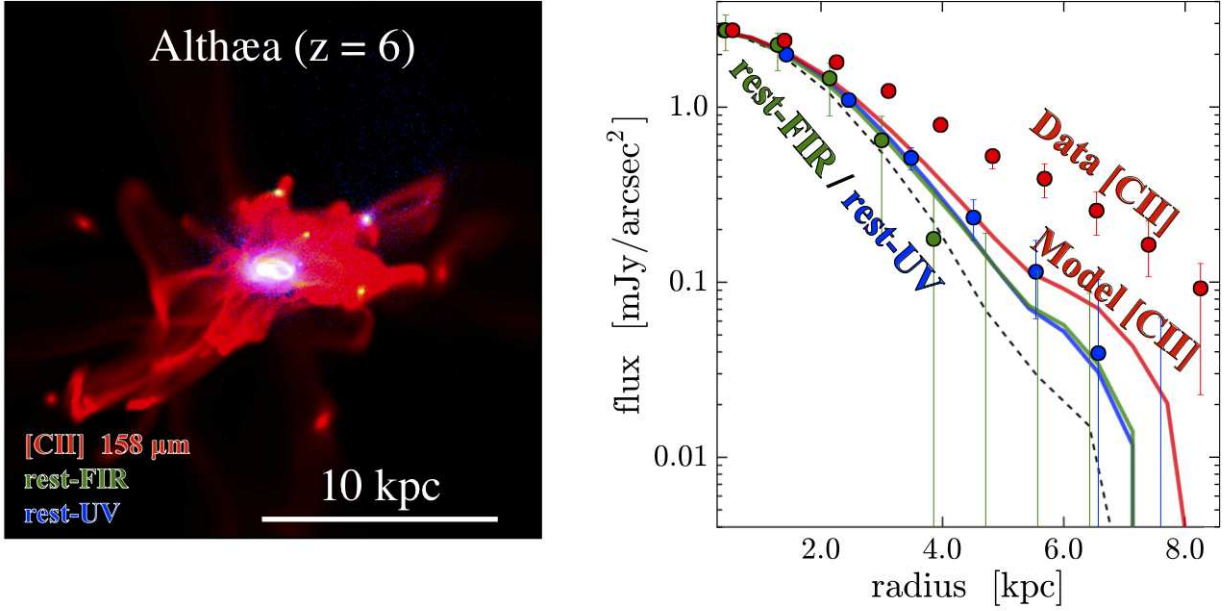


Figure 11. **Left)** $4'' \times 4''$ fake-color image for a star-forming galaxy of Althæa at $z = 6.0$ in the zoom-in simulation (red: [CII] line, green: rest-frame FIR continuum, blue: rest-frame UV continuum). **Right)** radial surface brightness profiles of the [CII] line (red curve), rest-frame FIR (green curve), and UV (blue curve) continuum emission estimated in the zoom-in simulation via the stacking procedure. Other symbols are assigned in the same manner as Figure 6.

The first scenario invokes satellite galaxies (Figure 12 A). If satellite galaxies exist around the central star-forming galaxies, the [CII] and Ly α line emission from the satellite galaxies will be observed as extended structures around the central galaxies. In this scenario, the extended halo size is determined by the spatial distribution of the satellite galaxies, which explains both extended components of the [CII] and Ly α line emission.

The second scenario is a PDR extended over CG scale (Figure 12 B). The ionizing photons ($h\nu > 13.6$ eV) from massive stars form the HII region on the central galactic scale. Far-ultraviolet (FUV) photons ($6 \text{ eV} < h\nu < 13.6$ eV) penetrate the surrounding ISM deeper than the ionizing photons, making the PDR extend more than the HII region. If the PDR is extended over the CG scale, the extended [CII] line emission is detected on the CG scale. Besides, the Ly α line emission is also spatially extended due to the resonance scattering by the neutral hydrogen in the surrounding ISM (e.g., Xue et al. 2017).

The third scenario is photoionization (Figure 12 C). This scenario is similar to scenario (B), but the HII region and the surrounding PDR is much more extended due to an existence of strong ionizing sources and/or the ISM properties differ from scenario (B). In this case, the Ly α line emission is extended due to the fluorescence (e.g., Cantalupo et al. 2005), instead of the resonance scattering in scenario (B). Although the carbon may be doubly ionized with less [CII] line emission near the ionizing source centers in the highly ionized ISM, such deficit of the [CII] line emission is consistent with the recent ALMA results that many star-forming galaxies at $z > 5$ do not always show clear [CII] line detections at the stellar-continuum positions (e.g., Carniani et al. 2018).

The fourth scenario is cold streams (Figure 12 D). Cos-

mological hydrodynamical simulations suggest that intense star-formation in high- z galaxies is fed by a dense and cold gas ($\sim 10^4$ K) that are dubbed cold streams (e.g., Dekel et al. 2009). The cold streams radiate [CII] as well as Ly α line emission powered by gravitational energy, and produce the extended [CII] and Ly α line emission around a galaxy. Moreover, the cold stream may cause shock heating which can also produce the [CII] and Ly α line emission.

The fifth scenario is outflow (Figure 12 E). In the outflow, the ionized carbon and hydrogen powered by the AGN and/or star-formation feedback produce the extended [CII] and Ly α line emission. The associated process of the shock heating may also contribute to radiating these line emission. Note that although we choose ALMA sources not reported as AGNs, we cannot rule out the possibility that our ALMA sources contain faint AGNs and/or have the past AGN activity.

In the following subsections, we discuss these possibilities based on the observational and theoretical results.

5.1. From Observational Results

In the observational results, the [CII] line is extended more than both the rest-frame FIR dust and UV continuum beyond the errors up to a radius of at least ~ 7 kpc (Figure 6). Assuming a constant [CII] line emissivity at a given stellar continuum (De Looze et al. 2014), the large gap between the radial profiles of the [CII] line and the stellar continuum indicates that the stellar continuum is not enough to explain the large part of the [CII] line emissivity of the [CII] halo.

Although the [CII] line emissivity may be changed from the central to halo areas at a given stellar continuum, the metallicity at such outer areas is expected to be $\sim 1\%$

A. Satellite Galaxies

B. CG-PDR

C. Photoionization

D. Cold Stream

E. Outflow

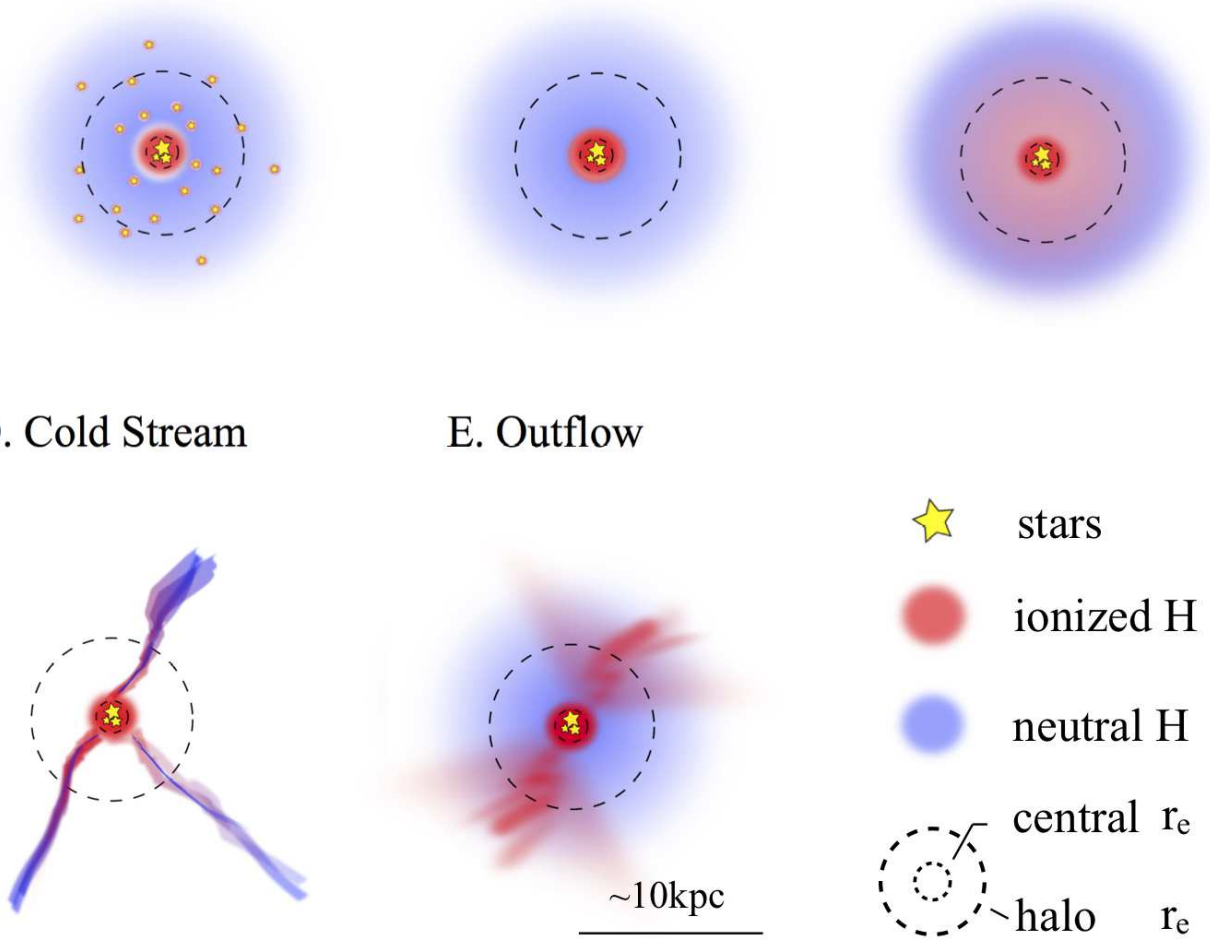


Figure 12. Illustrations of five possible origins of the $[\text{C II}]$ halo with the potential association of the $\text{Ly}\alpha$ halo. A) satellite galaxies; B) circum-galactic (CG) photodissociation region (PDR); C) photoionization; D) cold stream; and E) outflow. The blue and red shades show the neutral and ionized hydrogen in ISM and CGM. The yellow stars represent the star-forming regions. The inner and outer dashed circle denote the effective radii (r_e) of the central and halo components of the $[\text{C II}]$ line emission, respectively.

of the galaxy center (Pallottini et al. 2017a). Even if the stellar continuum at the halo areas is originated from low-mass, faint satellite galaxies, the mass–metallicity relation (Mannucci et al. 2010) likewise suggests the lower metallicity in the satellite galaxies than in the central galaxy. Because less metallicity makes the $[\text{C II}]$ line emissivity decreased at a given stellar continuum (Vallini et al. 2015), the different $[\text{C II}]$ line emissivities are furthermore difficult to explain the $[\text{C II}]$ halo by the stellar continuum. In fact, Figure 8 shows that the $L_{[\text{C II}]} / \text{SFR}_{\text{total}}$ ratio becomes higher towards halo areas where the high ratios cannot be explained either by the local star-forming or dwarf galaxies. Our observational results thus rule out the possibility of the scenario (A), supporting the rest of the four scenarios of (B)–(E).

5.2. From Theoretical Results

In the simulation results, the large part of the $[\text{C II}]$ line luminosity in the $[\text{C II}]$ halo is not reproduced (Fig-

ure 11). If the current assumptions related to the $[\text{C II}]$ line emissivity are correct, additional mechanism(s) are required to produce the extended $[\text{C II}]$ line emissivity in the simulation.

There are two possibilities of such additional mechanisms that are not included in the calculation of the $[\text{C II}]$ line emissivity in the simulation. The first possible mechanism is the shock heating (Appleton et al. 2013). Although the shock process is followed by the hydrodynamical calculation in the zoom-in simulation, the computation of the ionized carbon abundance in CLOUDY does not include the shock heating. Since the shock heating is caused in the galaxy merging or inflow/outflow processes, the scenarios of (A), (D), and (E) are supported. The second possible mechanism is the past/on-going AGN activities. The strong ionizing source of the past/on-going AGN activities forms a large area of the HII region and the surrounding PDR. Moreover, the AGN feedback may cause the shock heating, which also

contributes to the [CII] line emissivity. In this case, the scenarios of (C) and (E) are supported.

Note that if the pressures and/or radiations from the shock and the AGNs are strong, the carbon may be doubly ionized, where the [CII] line is rarely emitted. Therefore, it is hard to conclude whether the additional mechanisms of the shock and/or the AGNs are the major causes of the [CII] halo.

It should be also noted that 7 out of 9 sources in the ALMA-HST sample are placed at $5 < z < 6$, where the CMB effect is less than the zoom-in simulation results at $z = 6.0 - 7.2$. Because the CMB effect reduces the line luminosity from the diffuse component (e.g., da Cunha et al. 2013; Zhang et al. 2016), the slight difference in the redshift range may cause the insufficient [CII] line luminosity in the zoom-in simulation results.

5.3. Physical Origin of [CII] Halo

We summarize the possible scenarios for the physical origin of the [CII] halo based on the results of Sections 5.1–5.2. In the observational results, we rule out the scenario (A). In the zoom-in simulation results, it is hard to conclude which scenarios are most likely. The possible scenarios are thus (B), (C), (D), and (E) with the current best estimates of both observational and theoretical results.

Importantly, the outflow activities are required in all cases to enrich the carbon abundance in the primordial hydrogen gas surrounding the normal star-forming galaxies in the early Universe. Our results are thus the evidence of outflow remnants in these early star-forming galaxies.

There are two modes of outflows, hot-mode and cold-mode outflows. The hot-mode outflow is defined as the outflow of ionized hydrogen (hot) gas that is heated by supernova (SN) explosions, massive star/AGN radiation. The cold-mode outflow is the outflow of neutral hydrogen (cold) gas that is pushed by the radiative and kinetic pressures given by SNe, massive-stars, and AGNs. Here, the majority of [CII] line emission is radiated in neutral hydrogen (cold) gas clouds. Moreover, the cosmic time at $z \sim 5-7$ (~ 1 Gyr) is too short to produce the [CII]-emitting cold halos from hot gas expelled by the hot-mode outflow via recombination. Our finding of the [CII] halo implies that outflows in the early star-forming galaxies are dominated by cold-mode outflows.

Since we also find the similarity in the radial surface brightness profiles between the [CII] and Ly α halos (Figure 9), the physical origin of the [CII] halo may be related to the Ly α halo. Future deep observations of both [CII] and Ly α line emission for individual high- z galaxies are required to comprehensively understand the mechanism of the CGM metal enrichment with the theoretical simulations including the radiative transfers of these line emission.

6. SUMMARY

In this paper, we study the detail morphology of [CII] line emission via the ALMA visibility-based stacking method for normal star-forming galaxies whose [CII] line have been individually detected at $z = 5.153 - 7.142$. The visibility-based stacking achieves the deep and well-sampled visibility data in the uv -plane, which enables us to securely investigate the diffuse emission extended over

the circum-galactic environment. In conjunction with the deep HST/ H -band data, we examine the radial surface brightness profiles of the [CII] line, rest-frame FIR, and UV continuum emission. We then discuss the physical origin of the extended [CII] line emission. The major findings of this paper are summarized below.

1. The visibility-based stacking of our and archival deep ALMA data for 18 galaxies with $\text{SFR} \simeq 10-70 M_{\odot}$ at $z = 5.153 - 7.142$ produces 21σ and 10σ level detections at the peak for the [CII] line and dust continuum emission, respectively. The stacked [CII] line morphology is spatially extended more than that of the dust continuum. The radial surface brightness profiles of the [CII] line are extended up to a radius of ~ 10 -kpc scale at the 9.2σ level.
2. The HST/ H -band stacking for 9 out of the 18 [CII] line sources that are taken by the deep HST observations shows that the radial surface brightness profiles of the [CII] line is significantly extended more than that of the rest-frame UV as well as the rest-frame FIR continuum emission. We derive the radial ratio of $L_{[\text{CII}]} / \text{SFR}_{\text{total}}$, showing that the ratio becomes higher towards halo areas where the high ratios cannot be explained by the satellite galaxies.
3. The two component Sérsic+exponential profile fitting results indicate that the extended [CII] halo component has the scale length of 3.3 ± 0.1 kpc that is comparable to the Ly α halo universally found around the high- z star-forming galaxies. In the effective radius, the extended [CII] halo component is larger than the central galactic component by a factor of ~ 5 .
4. The state-of-art zoom-in simulation reproduces the radial surface brightness profile trends of the extended [CII] line emission and of the rest-frame FIR comparable to the rest-frame UV continuum emission. However, the simulation does not reproduce a large part of the [CII] line luminosity in the extended component, where the simulation may miss other mechanism(s) associated to the feedback process to form the extended [CII] halo component around the normal star-forming galaxies at $z \sim 6$.
5. Although there remain several possible scenarios that can give rise to [CII] line emission in the CGM, the outflow is required in any cases to enrich the carbon abundance in the primordial CGM around the early star-forming galaxies. Our results are thus the evidence of outflow remnants in the early star-forming galaxies.

We are grateful to Ivan Marti-Vidal and the Nordic ALMA Regional Center for providing us with helpful CASA software tools and advice on analyzing the data. We appreciate Tohru Nagao, Jeremy Blaizot, Peter Mitchell, Takashi Kojima, Shiro Mukae, Yuichi Harikane, and Rieko Momose for useful comments and suggestions. We are indebted for the support of the staff at the ALMA Regional Center. This paper makes

use of the following ALMA data: ADS/JAO. ALMA #2013.1.00815.S, #2015.1.00834.S, #2015.1.01111.S, #2015.1.01105, #2016.1.01240.S, #2012.1.00523.S, and #2012.1.00602.S. ALMA is a partnership of the ESO (representing its member states), NSF (USA) and NINS (Japan), together with NRC (Canada), MOST and ASIAA (Taiwan), and KASI (Republic of Korea), in co-operation with the Republic of Chile. The Joint ALMA Observatory is operated by the ESO, AUI/NRAO, and NAOJ. This study is supported by World Premier International Research Center Initiative (WPI Initiative), MEXT, Japan, and KAKENHI (15H02064, 17H01110, and 17H01114) Grant-in-Aid for Scientific Research (A) through Japan Society for the Promotion of Science (JSPS), the Grant-in-Aid for JSPS Research Fellow, the NAOJ ALMA Scientific Research Grant Number 2017-06B, and the Munich Institute for Astro- and Particle Physics (MIAPP) of the DFG cluster of excellence "Origin and Structure of the Universe". S.F. is supported by the ALMA Japan Research Grant of NAOJ Chile Observatory, NAOJ-ALMA-197. A.F. and R.J.I acknowledge supports from the ERC Advanced Grant INTERSTELLAR H2020/740120 and COSMIC ISM 321302, respectively.

REFERENCES

- Appleton, P. N., Guillard, P., Boulanger, F., et al. 2013, *ApJ*, 777, 66
- Aravena, M., Decarli, R., Walter, F., et al. 2016, *ApJ*, 833, 71
- Barisic, I., Faisst, A. L., Capak, P. L., et al. 2017, *ApJ*, 845, 41
- Behrens, C., Pallottini, A., Ferrara, A., Gallerani, S., & Vallini, L. 2018, *MNRAS*, 477, 552
- Bertin, E., & Arnouts, S. 1996, *A&A*, 117, 393
- Bischetti, M., Maiolino, R., Fiore, S. C. F., Piconcelli, E., & Fluetsch, A. 2018, *ArXiv e-prints*, arXiv:1806.00786
- Bouwens, R. J., van Dokkum, P. G., Illingworth, G. D., et al. 2017, *ArXiv e-prints*, arXiv:1711.02090
- Bowler, R. A. A., Bourne, N., Dunlop, J. S., McLure, R. M., & McLeod, D. J. 2018, *ArXiv e-prints*, arXiv:1802.05720
- Cantalupo, S., Porciani, C., Lilly, S. J., & Miniati, F. 2005, *ApJ*, 628, 61
- Capak, P. L., Carilli, C., Jones, G., et al. 2015, *Nature*, 522, 455
- Carniani, S., Maiolino, R., Amorin, R., et al. 2017, *ArXiv e-prints*, arXiv:1712.03985
- . 2018, *MNRAS*, arXiv:1712.03985
- Coppin, K., Halpern, M., Scott, D., et al. 2008, *MNRAS*, 384, 1597
- da Cunha, E., Groves, B., Walter, F., et al. 2013, *ApJ*, 766, 13
- De Looze, I., Cormier, D., Lebouteiller, V., et al. 2014, *A&A*, 568, A62
- Decarli, R., Walter, F., Venemans, B. P., et al. 2018, *ApJ*, 854, 97
- Dekel, A., Birnboim, Y., Engel, G., et al. 2009, *Nature*, 457, 451
- Dunlop, J. S., McLure, R. J., Biggs, A. D., et al. 2017, *MNRAS*, 466, 861
- Falgarone, E., Zwaan, M. A., Godard, B., et al. 2017, *Nature*, 548, 430
- Ferland, G. J., Chatzikos, M., Guzmán, F., et al. 2017, *Rev. Mexicana Astron. Astrofis.*, 53, 385
- Fujimoto, S., Ouchi, M., Ono, Y., et al. 2016, *ApJS*, 222, 1
- Fujimoto, S., Ouchi, M., Shibuya, T., & Nagai, H. 2017, *ApJ*, 850, 1
- Fujimoto, S., Ouchi, M., Kohno, K., et al. 2018, *ApJ*, 861, 7
- Gaia Collaboration, Brown, A. G. A., Vallenari, A., et al. 2018, *A&A*, 616, A1
- George, R. D., Ivison, R. J., Smail, I., et al. 2014, *MNRAS*, 442, 1877
- Harikane, Y., Ouchi, M., Ono, Y., et al. 2018, *PASJ*, 70, S11
- Hayatsu, N. H., Matsuda, Y., Umehata, H., et al. 2017, *PASJ*, 69, 45
- Hodge, J. A., Swinbank, A. M., Simpson, J. M., et al. 2016, *ApJ*, 833, 103
- Ikarashi, S., Ivison, R. J., Caputi, K. I., et al. 2015, *ApJ*, 810, 133
- Ilbert, O., McCracken, H. J., Le Fèvre, O., et al. 2013, *A&A*, 556, A55
- Ivison, R. J., Papadopoulos, P. P., Smail, I., et al. 2011, *MNRAS*, 412, 1913
- Jones, G. C., Willott, C. J., Carilli, C. L., et al. 2017, *ApJ*, 845, 175
- Kawamata, R., Ishigaki, M., Shimasaku, K., et al. 2018, *ApJ*, 855, 4
- Knudsen, K. K., Richard, J., Kneib, J.-P., et al. 2016, *MNRAS*, 462, L6
- Leclercq, F., Bacon, R., Wisotzki, L., et al. 2017, *A&A*, 608, A8
- Lindroos, L., Knudsen, K. K., Vlemmings, W., Conway, J., & Martí-Vidal, I. 2015, *MNRAS*, 446, 3502
- Maiolino, R., Gallerani, S., Neri, R., et al. 2012, *MNRAS*, 425, L66
- Maiolino, R., Carniani, S., Fontana, A., et al. 2015, *MNRAS*, 452, 54
- Mannucci, F., Cresci, G., Maiolino, R., Marconi, A., & Gnerucci, A. 2010, *MNRAS*, 408, 2115
- Matsuda, Y., Yamada, T., Hayashino, T., et al. 2012, *MNRAS*, 425, 878
- Matthee, J., Sobral, D., Santos, S., et al. 2015, *MNRAS*, 451, 400
- Matthee, J., Sobral, D., Boone, F., et al. 2017, *ApJ*, 851, 145
- McMullin, J. P., Waters, B., Schiebel, D., Young, W., & Golap, K. 2007, in *Astronomical Society of the Pacific Conference Series*, Vol. 376, *Astronomical Data Analysis Software and Systems XVI*, ed. R. A. Shaw, F. Hill, & D. J. Bell, 127
- Momose, R., Ouchi, M., Nakajima, K., et al. 2016, *MNRAS*, 457, 2318
- Murphy, E. J., Condon, J. J., Schinnerer, E., et al. 2011, *ApJ*, 737, 67
- Oesch, P. A., Bouwens, R. J., Carollo, C. M., et al. 2010, *ApJ*, 725, L150
- Oke, J. B., & Gunn, J. E. 1983, *ApJ*, 266, 713
- Ono, Y., Ouchi, M., Curtis-Lake, E., et al. 2013, *ApJ*, 777, 155
- Ouchi, M., Shimasaku, K., Akiyama, M., et al. 2008, *ApJS*, 176, 301
- Ouchi, M., Mobasher, B., Shimasaku, K., et al. 2009, *ApJ*, 706, 1136
- Pallottini, A., Ferrara, A., Bovino, S., et al. 2017a, *MNRAS*, 471, 4128
- Pallottini, A., Ferrara, A., Gallerani, S., et al. 2017b, *MNRAS*, 465, 2540
- Pallottini, A., Gallerani, S., Ferrara, A., et al. 2015, *MNRAS*, 453, 1898
- Peng, C. Y., Ho, L. C., Impey, C. D., & Rix, H.-W. 2010, *AJ*, 139, 2097
- Pentericci, L., Carniani, S., Castellano, M., et al. 2016, *ApJ*, 829, L11
- Planck Collaboration, Abergel, A., Ade, P. A. R., et al. 2011, *A&A*, 536, A21
- Rujopakarn, W., Dunlop, J. S., Rieke, G. H., et al. 2016, *ApJ*, 833, 12
- Sérsic, J. L. 1963, *Boletín de la Asociación Argentina de Astronomía La Plata Argentina*, 6, 41
- Shibuya, T., Ouchi, M., & Harikane, Y. 2015, *ApJS*, 219, 15
- Simpson, J. M., Smail, I., Swinbank, A. M., et al. 2015, *ApJ*, 799, 81
- Skelton, R. E., Whitaker, K. E., Momcheva, I. G., et al. 2014, *ApJS*, 214, 24
- Smit, R., Bouwens, R. J., Labbé, I., et al. 2014, *ApJ*, 784, 58
- Smit, R., Bouwens, R. J., Carniani, S., et al. 2018, *Nature*, 553, 178
- Stacey, G. J., Geis, N., Genzel, R., et al. 1991, *ApJ*, 373, 423
- Steidel, C. C., Bogosavljević, M., Shapley, A. E., et al. 2011, *ApJ*, 736, 160
- Vallini, L., Gallerani, S., Ferrara, A., Pallottini, A., & Yue, B. 2015, *ApJ*, 813, 36
- Watson, D., Christensen, L., Kraiberg Knudsen, K., et al. 2015, *ArXiv e-prints*, arXiv:1503.00002
- Willott, C. J., Carilli, C. L., Wagg, J., & Wang, R. 2015, *ApJ*, 807, 180
- Willott, C. J., Omont, A., & Bergeron, J. 2013, *ApJ*, 770, 13
- Xue, R., Lee, K.-S., Dey, A., et al. 2017, *ApJ*, 837, 172
- Zhang, Z.-Y., Papadopoulos, P. P., Ivison, R. J., et al. 2016, *Royal Society Open Science*, 3, 160025